Comparative Performance of M-MCM-41 (M: Cu, Co, Ni, Pd, Zn and Sn) Catalysts for Steam Reforming of Methanol

Richard Y. Abrokwah[a], Vishwanath G. Deshmane[b,c*], Debasish Kuila[c*]

[a]Department of Energy and Environmental Systems

[b]Department of Chemical, Biological and Bioengineering

[c]Department of Chemistry

North Carolina Agricultural and Technical State University

Greensboro, NC 27411 USA

* To whom correspondence should be addressed.

Phone: (336)285-2243. Fax: (336)334-7417.

E-mail: dkuila@ncat.edu; vdeshman@aggies.ncat.edu

Abstract

One-pot hydrothermal procedure was used to synthesize high surface area M-MCM-41 (M: Cu, Co, Ni, Pd, Zn, and Sn) nanocatalysts. The M-MCM-41 catalysts containing 10wt% of different metals were examined to evaluate the performance of individual metals in steam reforming of methanol (SRM) in terms of activity, selectivity and long term stability under similar operating conditions. The fresh and spent catalysts were characterized using BET, XRD, TGA-DSC, TEM, TPR, ICP-OES, EDX, Raman, and FTIR analytical techniques. Cu-MCM-41 showed the best performance in terms of activity and selectivity among the different catalysts investigated in this study. The overall SRM reactivity trend for different metals based on methanol conversion followed the order: Cu-MCM-41 > Pd-MCM-41 > Sn-MCM-41 > Ni-MCM-41 ≈ Zn-MCM-41 > Co-MCM-41. The catalytic performance of Cu-MCM-41 at 250 °C using 1:3 methanol-water mole ratios showed 100% H_2 selectivity, ~6% CO, and no methane formation. The time-on-stream studies conducted continuously for 40 h at 300 °C revealed that Cu-MCM-41 was the most stable catalysts and displayed consistent steady state conversion (up to74%). The SRM activity of Pd, Sn and Zn was comparatively better; however, they deactivated steadily with time. Although coking was a major factor in deactivation of the catalysts, degradation of the mesoporous structure and thermal sintering appeared to play an influential role in deactivation, particularly in the case of Sn-MCM-41.

Keywords: One-pot synthesis; metal-MCM-41 catalysts; steam reforming of methanol; catalyst stability; Cu, Co, Ni, Pd, Zn, and Sn.

.

1. Introduction

Transition from non-replenishable fossil fuel energy to alternative clean energy such as hydrogen is no longer an academic debate. Catalytic steam reforming of renewable alcohols (e.g. methanol, glycerol and ethanol) is a highly favored route to produce hydrogen to generate electricity, as well as, to power portable electronic gadgets and vehicles using fuel cell technology. Traditionally, copper based catalysts supported on Al_2O_3, ZnO and ZrO_2 have been studied and used for commercial alcohol steam reforming processes [1-3]. Recently, Zhang et al. [4] showed that Cu supported on three different supports (CeO_2, ZrO_2 and CeO_2-ZrO_2) exhibited significant contrast in catalytic performance towards steam reforming of methanol. Hirunsit and Faungnawakij demonstrated that Cu-based spinel-lattice catalysts possess high thermal stability which suppresses Cu sintering at high reaction temperature [5]. In contrast, we and others [6-10] have focused on the use of high surface area mesoporous supports (e.g. MCM-41, SBA-15, and TiO_2) for steam reforming, which tend to avail a high catalytic surface area with well defined large pore sizes mitigating the catalyst deactivation (via sintering) by enhancing uniform dispersion of the active metal particles. Recently, the versatility and robustness of these mesoporous silica nanomaterials (MSNs) as inorganic supports have been extensively and critically reviewed byYamamoto et al [11] and other research groups [12, 13]. The researchers pointed out several advantages of these materials including biocompatibility, high rigidity, high surface areas, tunable mesopores and easy functionalization of their pore interiors and surfaces with drugs, organic molecules and metal oxides.

Several catalytic systems have been used over the years for steam reforming reactions. Riva et al. [14] elucidated that cobalt (Co) catalysts supported by TiO_2 and SiO_2 exhibit remarkable differences in their binding energy. They inferred that Co-TiO_2 interactions were strong and made

Co very resistant to reduction while the weaker Co-SiO_2 interactions resulted in sintering and low reactivity. The high reactivity of nickel (Ni) supported on MCM-41, La_2O_3, Al_2O_3, yttria-stabilised zirconia (YSZ), and MgO catalysts in steam reforming reactions to produce hydrogen have also been studied extensively [15-17]. Incorporation of tin (Sn) and zinc (Zn) are reported to promote the water-gas shift and/or methanation reactions [3, 18, 19]. Palladium (Pd) is generally used as a promoter to bolster the conversion of steam reforming reactions due to its inherent ability to (i) improve reducibility of other metals and (ii) form substitutional and intermetallic alloys, particularly with Zn and Ni [20].

While the aforementioned studies are certainly useful and informative, the catalysts (different combinations of the metals and supports) were synthesized using different approaches, and utilized for different feedstocks under different steam reforming experimental conditions. Therefore, a comparative in-depth study of the intrinsic physicochemical properties and catalytic performance of supported metals prepared by one particular method, and tested under similar experimental conditions could provide a platform to get invaluable insights into the reasons for any stark contrasts in their catalytic behaviors. In addition, such a thorough investigation of each metal-support system could predict how they could be stoichiometrically combined in tailoring efficient and robust multi-metallic catalytic systems. In this study, we report synthesis of mesoporous catalysts using a one-pot hydrothermal method, and insights into how the interactions between each individual metal and MCM-41 support impact their SRM performance under identical experimental conditions in a packed bed reactor. The contrast in behavior of each metal towards methanol conversion, selectivity for hydrogen, methane, carbon monoxide and carbon dioxide during steam reforming of methanol, and the stability of the catalysts are discussed.

2. Experimental

2.1. Materials and Methods

All the reagents utilized were analytical grade and used without further purification. Tetramethylorthosilicate, 99% (TMOS) and ammonium hydroxide, ACS (American Chemical Society) reagents, were purchased from Acros Organics, New Jersey, USA. Cetyltrimethylammoniumbromide (CTAB), $Ni(NO_3)_2.6H_2O$, $Cu(NO_3)_2.2.5H_2O$, $CoCl_2.6H_2O$, $Pd(NO_3)_2$, $Zn(NO_3)_2.6H_2O$ and $SnCl_2.2H_2O$ were procured from Sigma-Aldrich, Missouri, USA. Ethanol anhydrous and acetone, ACS reagents were purchased from Fischer Scientific, New Jersey, USA. The de-ionized water used for all experiments was purified using a Mill-Q Advantage A10 Elix 5 system obtained from Millipore Corporation (Bedford, MA, USA).

2.2. Catalyst Synthesis

MCM-41 supported mono-metallic (M-MCM-41; M: Cu, Co, Ni, Pd, Sn, and Zn) catalysts were synthesized using a one-pot hydrothermal procedure [21]. The molar composition ratios of the reagents used were: 1TMOS: 0.13CTAB: $130.6H_2O$: 20Ethanol. The quantity of metal precursors used was based on the expected 10wt% metal loading in the final mesoporous matrix. Since all the synthesized catalysts have 10wt% metal loading, it is not included in the designation of the catalysts in rest of the writeup. In a typical synthesis, the surfactant (CTAB) was weighed, dissolved in de-ionized water at 30 °C and stirred to get a colorless solution A. Another solution designated B was prepared by dissolving the metal precursors in ethanol. Solution B was gently poured into solution A and stirred for 30 min. To this mixture, the limiting reagent (TMOS) was added drop-wise and stirred continuously for another 30 min. Ammonium hydroxide was then added drop-wise to precipitate the metal hydroxides at pH 10. The solution was then stirred for another 3 h and then aged in an oven at 65 °C for 18 h. The obtained precipitate was washed with

de-ionized water and ethanol to get a filtrate of pH 7. The filtered material was air dried for ~24 h, followed by oven drying at 110 °C for 24 h. The catalyst was calcined at 550 °C for 16 h at a heating and cooling rate of 2 °C/min to remove the surfactant (CTAB).

2.3. Catalyst Characterization

Specific surface area, pore-size, and pore volume of the catalysts were determined using a Quantachrome NOVA 2200e instrument (Quantachrome Instruments, Boynton Beach, FL, USA). The surface area was calculated using the Brunauer-Emmett-Teller (BET) equation from the adsorption branch of the isotherm in a relative pressure (P/P_0) range of 0.07–0.3. The average BET surface area of $1.0 \pm .002$ m^2 was determined with a confidence level of 95%. The total pore volume was evaluated depending on the amount of N_2 adsorbed at a $P/P_0 = 1$. The pore size distribution and average pore sizes were determined by means of a non-local density functional theory (NLDFT) method [22].

The H_2 temperature programmed reduction (TPR) analysis was carried out with the AutoChem II 2920 Chemical Analyzer from Micromeritics Instrument Corp. (Norcross, GA, USA) equipped with a TCD detector. In a typical analysis, gas stream (10% H_2/Ar) at a flow rate of 50 ml/min was flown through ~30 mg of catalyst while the temperature was increased from room temperature to 1000 ºC at a 10 ºC/min ramp rate.

The small and wide angle powder X-ray diffractions(XRD) were recorded using a D8 discover x-ray diffractometer from Bruker (Bruker Optics, Inc., Billerica, MA) with PSD detector, using Cu Kα radiation generated at 40 mA and 40 kV at the scanning rate of 0.014°/s. The crystal sizes of the metal oxides were determined using Scherrer equation.

$$\tau = \frac{0.9\lambda}{\beta \cdot \cos\theta} \quad (1)$$

Where, τ is the crystal size, λ is the wavelength of the Cu Kα radiation, β is the full width half maximum and θ is the Braggs diffraction angle. Thermogravimetric (TGA) and differential scanning calorimetry analyses (DSC) were performed using the SDT Q600 V20.4 Build 14 system (TA Instruments, New Castle, DE, USA) at a heating rate of 10 °C/min with air flow rate of 100 ml/min. The empirical elemental compositions were estimated using inductively coupled plasma optical emission spectroscopy (ICP-OES) Agilent 710-ES spectrometer and energy dispersive X-ray spectroscopy (EDX)-Zeiss EVO LS10 scanning electron microscopy (SEM) equipped with Oxford INCA X-act detector. The ICP-OES samples were prepared by dissolving 75 mg of the catalyst in a mixture of 2 ml hydrofluoric acid (51%) and 3 ml nitric acid (68%), and heated gently to 80 °C until complete dissolution of the catalysts. Prior to elemental analysis, the metal solution was diluted with 1000 ml de-ionized water and filtered.

The Fourier transform infrared (FTIR) spectra were recorded using Shimadzu IR Prestige-21 Fourier transform infrared 8300 spectrometer equipped with liquid-N_2–cooled mercury-cadmium-telluride (MCT) detector. To maintain a suitable balance between the signal resolution and ripple size effects, the Happ-Genzel apodization function was used. The KBr pelletization method was employed for the sample preparation and the spectrum was recorded at room temperature in the range of 400 to 4000 cm^{-1} at 4 cm^{-1} resolution.

Raman spectra of the samples were recorded using a Horiba XploRA Raman Confocal Microscope System (Horiba JobinYvon) equipped with an air cooled charge-coupled-device (CCD) detector and integrated with an internal laser of 785 nm. The catalysts were placed on a very clean microscopic slide for spectral acquisition, focused with a laser at 50x working distance objective and the spectra were recorded using 600 groves (mm) grating. The background was then subtracted from the acquired spectra.

The morphology of catalyst was studied with the Zeiss Libra 120 (©Carl Zeiss NTS GmbH, Oberkochen, Germany) transmission electron microscope (TEM) operated at an accelerating voltage of 120 kV. First, a small quantity of the catalyst was dispersed in 3 ml of ethanol and sonicated for few minutes. Then, a Lacey carbon coated grid, 300 mesh size, with 63μm grid size was slowly dipped several times in the mixture. The grid was then placed in a sample holder and dried in an oven at 100 °C for 12 h.

2.4. Catalyst Activity Test

The SRM tests were performed at atmospheric pressure in a continuous up flow stainless steel fixed bed reactor (Tube ID: 6.22 mm). A methanol/water molar ratio of 1/3 and a GHSV of 2838 h^{-1} at STP was maintained for all the reactions. Catalysts were activated *ex-situ* in a tubular furnace using 10% H_2/Ar at 550 ºC for 5 h. The activated catalyst was diluted with white quartz sand (50-70 mesh size) in a catalyst/sand volume ratio of 2:1 to increase the interparticle porosity and decrease the pressure drop across the reactor. Prior to SRM experiments, the catalyst was further activated *in-situ* at 350 °C for 1 h under 10% H_2/Ar environment. The Agilent 7890B GC equipped with thermal conductivity detector (TCD) and flame ionization detector (FID) were used for quantitative estimation of the product gases, and collected condensate, respectively. The gaseous products were separated using Restek Shin Carbon (2 m x 2 mm x 1/8") packed column and the cold trapped condensate was analysed with an Agilent DB-1 (60 m x 250 μm x 1 μm) capillary column with He as the carrier gas. The methanol conversion and selectivity towards reformate gases were evaluated using **Eqs. 2-4** as follows:

$$Conversion_{Methanol} = \frac{CH_3OH\ moles\ converted}{CH_3OH\ moles\ used} \times 100\% \quad (2)$$

$$S_{CO/CO2/CH4} = \frac{CO/CO2/CH4\ moles\ in\ product}{(CO_2 + CO + CH4)\ moles\ in\ product} \times 100\% \quad (3)$$

$$S_{H_2} = \frac{H_2\ moles\ in\ product}{(moles\ of\ H_2 + 2\ X\ moles\ of\ CH_4)\ in\ product} \times 100\% \quad (4)$$

2.5 Catalyst Stability Tests

Catalysts stability tests were performed with freshly reduced catalyst for continuous 40 h under the same conditions as described in **section 2.4**. The sand and spent catalysts were separated using 300 mesh screen (150 µm opening size). The spent catalysts were subjected to various characterizations such as BET, XRD and TGA-DSC.

3. Results and Discussion

3.1. Thermal Behavior and Template Removal Analysis of M-MCM-41 Samples

The TGA and DSC analyses were performed simultaneously to ascertain the thermal behavior of the samples. **Fig. 1** shows the TGA-DSC profiles of as-synthesized pure MCM-41 and M-MCM-41 samples recorded under air.

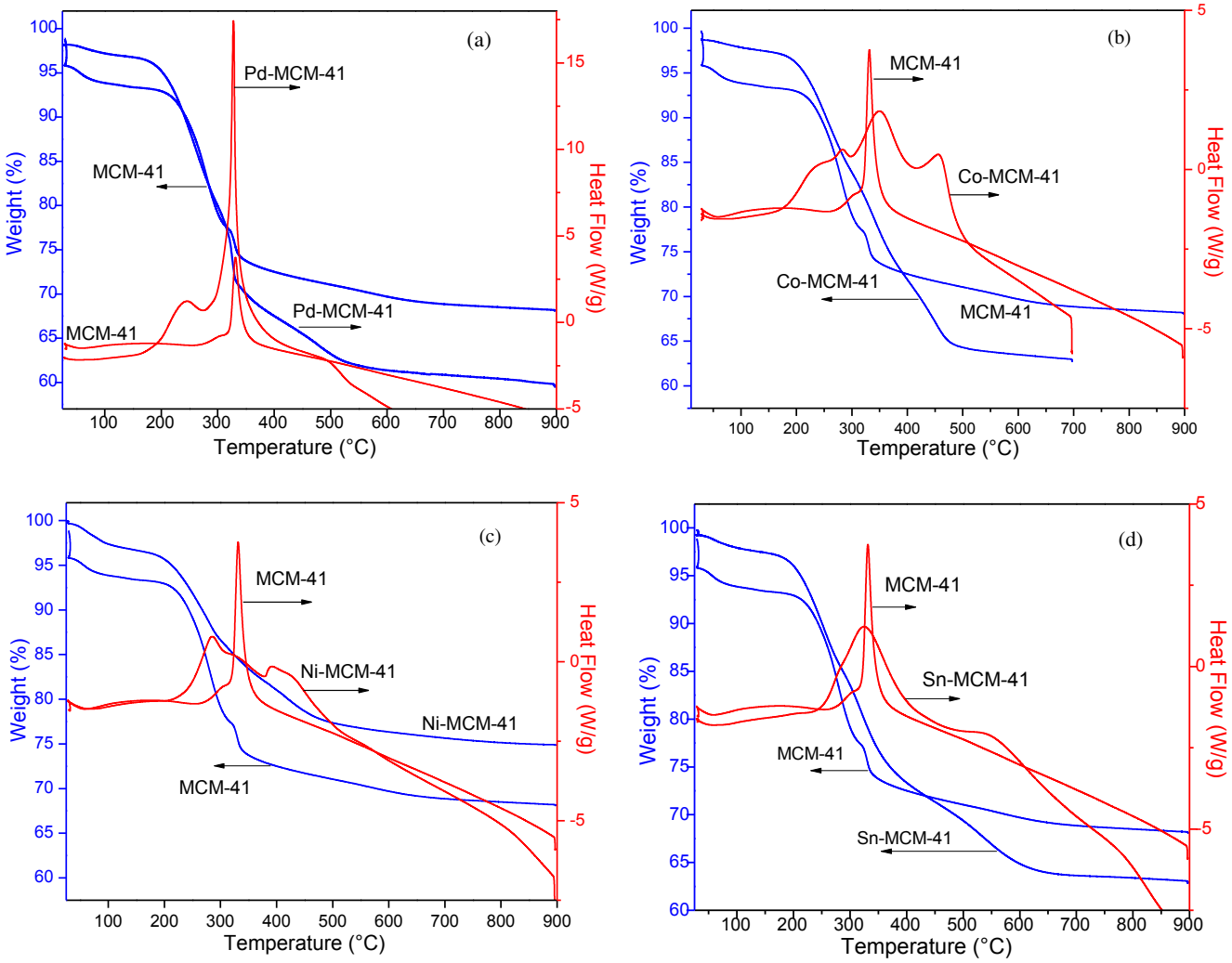

Fig. 1: TGA-DSC thermograms of as-synthesized: (a) Pd-MCM-41, (b) Co-MCM-41, (c) Ni-MCM-41, and (d) Sn-MCM-41 overallped with MCM-41

In all cases, the DSC profiles progressed with a sharp exothermic peak between 280 and 350 °C associated with notable weight loss that can be attributed to decomposition of the template (CTAB) used in MCM-41 synthesis. The weight loss before 200 °C is related to vaporization of physiosorbed water and/or gas molecules on the catalyst surface. Another exothermic weight loss between 200-280 °C for Pd-MCM-41 is ascribed to the decomposition of $Pd(NO_3)_2$ precursor and traces of $Pd(NH_3)_2$ complex arising from NH_3 used for precipitation of the sample during synthesis

[23-25]. The Co-MCM-41 samples showed two distinct exothermic peaks apart from the strong peak observed due to CTAB decomposition at about 350 °C. The first broader thermogram representing ~3% gradual weight loss from 200-300 °C is ascribed to decomposition of the precursor $CoCl_2.6H_2O$, while the second sharper peak with ~5% weight loss between 450-500 °C is due to decomposition of $Co(OH)_2$ to CoO in the silica matrix [26]. In the thermograms of Ni-MCM-41 samples, ~2% weight loss in the range of 400-500 °C could be associated with the decomposition of $Ni(OH)_2$. This is consistent with the observations made by Li and Liu [27] for the decomposition of $Ni(OH)_2$ to NiO between 335 and 500 °C. The profile for Sn-MCM-41 (which had a similar thermal degradation profile as Zn-MCM-41, data not provided) showed a minute weight loss at 550 °C, most likely due to the presence of polymeric Sn hydroxide groups which normally decompose to tin oxides at temperature ≥ 500 °C [28]. The steady minimal weight loss which occurred above 600 °C for all samples could be ascribed to condensation of intramolecular water molecules to form the Si-O-Si-O-Si framework [29].

3.2. Textural Properties Evaluation of Calcined Materials

In order to evaluate the textural properties of the catalysts, a nitrogen physiosorption analysis was performed. **Table 1** summarizes the textural properties of MCM-41 support, calcined and spent M-MCM-41 catalysts. While pure MCM-41 showed surface area of ~1039 m^2/g, the surface areas for 10wt% metal loaidngs were observed in the range of 795 to 1000m^2/g, depending on the type of metal. Usually, the addition of metal fills the pores making them inaccessible to N_2 (adsorbate) molecules and thus decreases the surface area. The pore diameter increased slightly from 3.2 nm to an average of 3.65 nm upon incorporation of the metals. This can be attributed to the plugging of smaller pores by metal particles as well as interference of the formation of ordered mesopores by the metal ions, which also leads to a decline in surface area.

Table1: BET surface area, pore size and pore volume of calcined and spent catalysts

MCM41 Supported Catalysts	Surface Area[1] (m^2/g)	Surface Area[1] (m^2/g) after 40h Reaction	Pore Size[2] (nm)	Pore Size[2] (nm) after 40h Reaction	Pore Volume[3] (cm^3/g)	Pore Volume[3] (cm^3/g) after 40h Reaction
MCM-41	1039.2	-	3.2	-	0.75	-
Ni-MCM-41	824.6	543.0	3.8	3.7	0.84	0.76
Cu-MCM-41	795.7	444.4	3.7	3.6	0.62	0.42
Pd-MCM-41	1078.8	729.4	3.5	3.5	0.82	0.56
Sn-MCM-41	1009.3	668.2	3.3	3.2	0.77	0.51
Co-MCM-41	815.8	447.1	3.6	3.8	0.79	0.66
Zn-MCM-41	800.3	494.1	3.5	2.6	0.62	0.39

The total pore volume varied from 0.619 –0.843 cm^3/g, indicating differences in the pore volume and shapes of the mesopores.The N_2 adsorption-desorption isotherms of all the catalysts in **Fig. 2** show a typical type IV isotherm and H1 hysteresis loop (based on the empirical IUPAC classification) which are indicative of mesoporous materials. The point of inflection at relative pressure of (P/P_0 = 0-0.2) represents the completion of monolayer coverage by N_2 – adsorbate. The uptake in N_2 adsorption from P/P_0 = 0.2-0.4 corresponds to N_2 condensation within the ordered mesopores of the MCM-41 framework. The steepness of this step (P/P_0 = 0.2-0.4) emphasizes the narrow ordered pore size distribution of the MCM-41. It is worth noting that the steepness decreased upon incorporation of metals, suggesting some loss of the ordered structure upon metal addition. The plateau at high relative pressures (P/P_0 = 0.4 -0.85) is attributed to the multilayer N_2 adsorption. Finally, the sharp N_2 adsorption at higher relative pressues (P/P_0> 0.9) associated with a small hysteresis loop is usually ascribed to N_2 condensation in the interparticle pores [30].

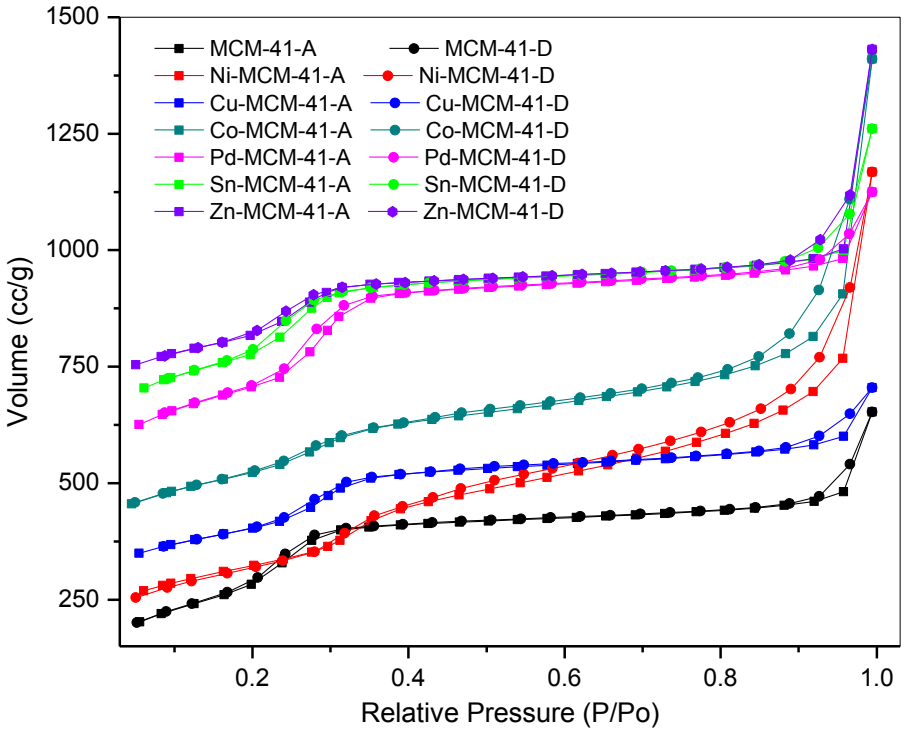

Fig. 2: N_2 adsorption-desorption isotherms of M-MCM-41 catalysts

3.3. Powder X-ray Diffraction Studies of Calcined Materials

The powder XRD method was used for structural phase identification, determination of lattice parameters such as the crystallite sizes and evaluation of changes in the shapes and sizes of the ordered mesopores. **Fig. 3(a)** shows the small angle powder XRD spectra of calcined M-MCM-41 catalysts. The mesoporous structures of M-MCM-41 samples inferred by the N_2 physisorption isotherms in **Fig. 2** are consistent with the XRD studies. The variations in the XRD peak intensities and positions due to different metals are clearly observed in **Fig. 3(a)**. While the XRD spectra of pure MCM-41 and Pd-MCM-41 showed intense resolved diffraction peaks, Zn-MCM-41 showed least intensity peak; in 2θ value range of ~1.5-2.5°, which could be indexed to (100) reflections. Additionally, two low intensity peaks for (110) and (200) reflections centered at ~4.4° and ~5.2°, respectively, were observed only for MCM-41 and Pd-MCM-41. Since the catalysts are prepared

using one-pot method, the decreased order of MCM-41 upon metal addition indicates that the metal ion could be interfering with ordered structure formation during the synthesis.

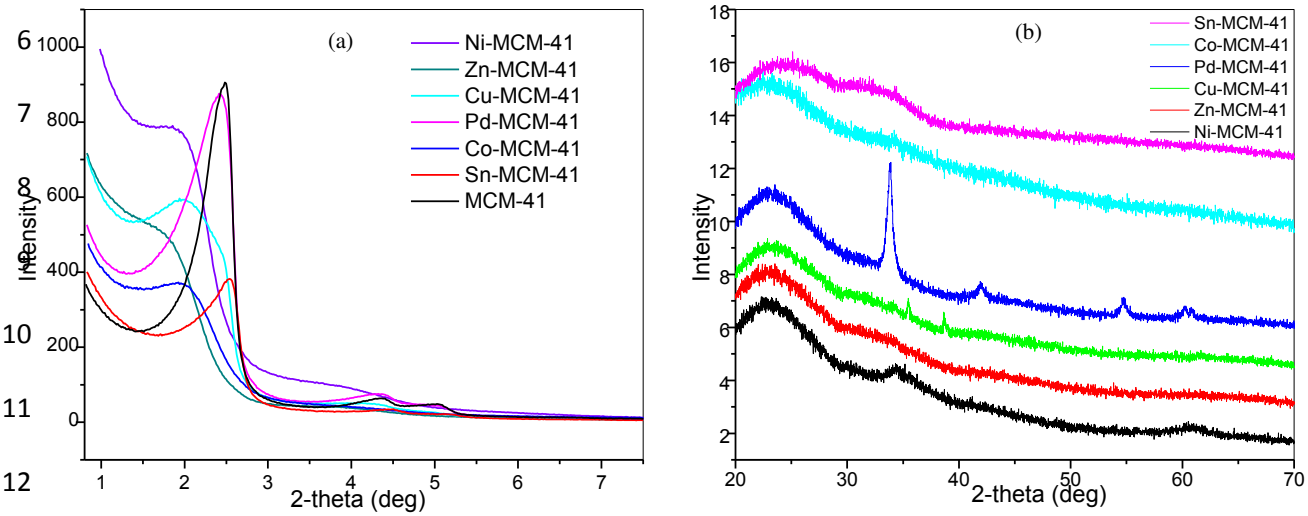

Fig. 3: (a) SAXRD, and (b) WAXRD patterns of calcined M-MCM-41catalysts

The results shown in Fig. 3 (a) also suggest that the extent of this influence is different for different metals on the MCM-41 structure. For example, while Pd showed no effect on mesoporous structure, Zn affected it the most. The relatively intense peaks of Pd-MCM-41 and Sn-MCM-41 suggest that they are comparatively the most ordered mesoporous catalysts, and consequently exhibited the exceptionally high surface areas showed by BET analysis **(Table 1).** The peak intensities of Co-, Zn-, Cu- and Ni-MCM-41 catalysts were much broader and weaker, and shifted towards a lower 2θ value. While the weaker intensities implied the loss of some degree of ordered structure, the lower angle shift indicated an increase in pore sizes. This observation corroborates our inference that the sharpness of the pore filling step (P/P_0 = 0.2-0.4) of the N_2 sorption isotherm

(Fig. 2) decreases with metal addition due to significant decline in the long range order of the MCM-41 framework (**Fig. 3a**).

The wide angle X-ray diffraction patterns of the calcined M-MCM-41 catalysts are shown in **Fig. 3 (b)**. The XRD spectra of Cu-MCM-41 samples exhibited two weak diffraction peaks at 2θ values around 35.6º and 38.9º attributed to the CuO crystallites phase (JCPDS 80-1917). PdO-crystallites exhibited intense diffraction peak centered at 2θ value of 33.9º indexed to (101) reflections, followed by weaker difractions at 42.3º, 55º, 61.1º and 72.1º indexed to (110), (112), (200), and (211) reflections (JCPDS 75-584), respectively [31]. The remarkably intense diffraction peaks observed for Pd-MCM-41 could be due to large electron density of Pd [32, 33]. The crystal sizes of CuO and PdO calculated by the Scherrer's equation are 14.2 nm and 15.8 nm, respectively. No discernible diffraction peaks are observed for oxides of Sn, Ni, Co and Zn. This can be attributed to three possibilities: (i) the nanocyratalline oxides are embedded in the pore walls of the matrix, hence insufficiently exposed and thereby minimizing diffractions, (ii) nanocrystalline nature of the particles; making them x-ray amorphous, and (iii) preferential orientation of the metal particles in the MCM-41 matrix resulting in little or no diffractions.

3.4. SEM-EDX Analysis

SEM-EDX analysis was carried out to examine the distribution of metals in MCM-41 framework. **Fig. 4** shows the EDX-SEM elemental mapping of the catalysts. A close examination of the images reveal that Cu, Pd, Sn and Zn particles (red dots) were highly dispersed throughout the MCM-41 framework (gray background). On the other hand, Co and Ni particles were comparatively less dispersed in the support and showed signs of agglomeration. A uniform distribution of the metal particles bolsters stability by retarding catalyst deactivation caused via metal particles sintering.

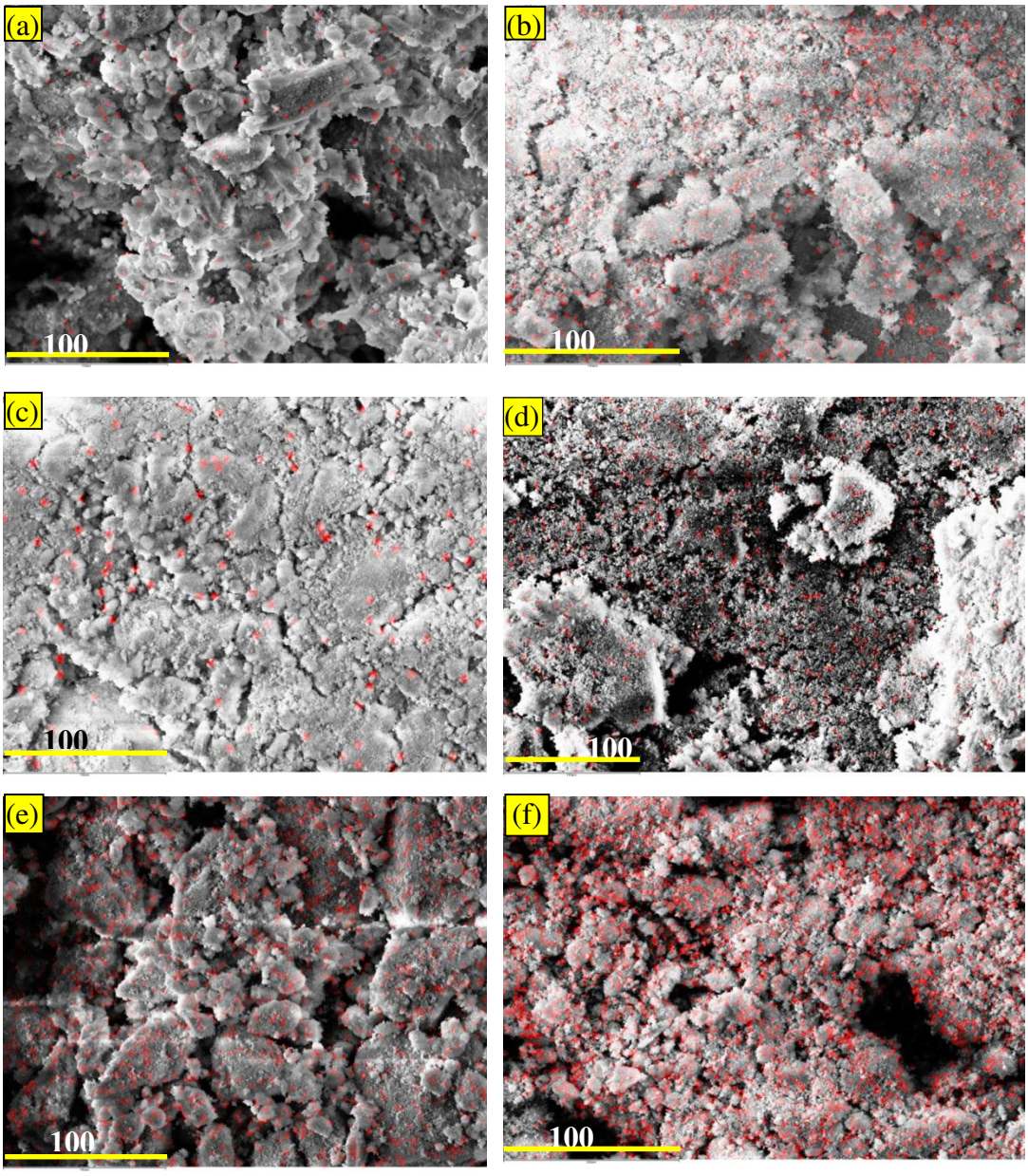

Fig. 4: EDX-SEM elemental mapping of MCM-41 catalysts (Red Dots): (a) Co, (b) Cu, (c) Ni, (d) Pd, (e) Sn, and (f) Zn

3.5. Tranmission Electron Microscopic Imaging

TEM imaging was performed to corroborate the BET and XRD results, and to obtain an approximate value of the pore and metal particle sizes of the calcined catalysts. **Fig. 5(a) and (b)**

show the typical high resolution TEM images of the calcined pure MCM-41 and Pd-MCM-41, respectively.

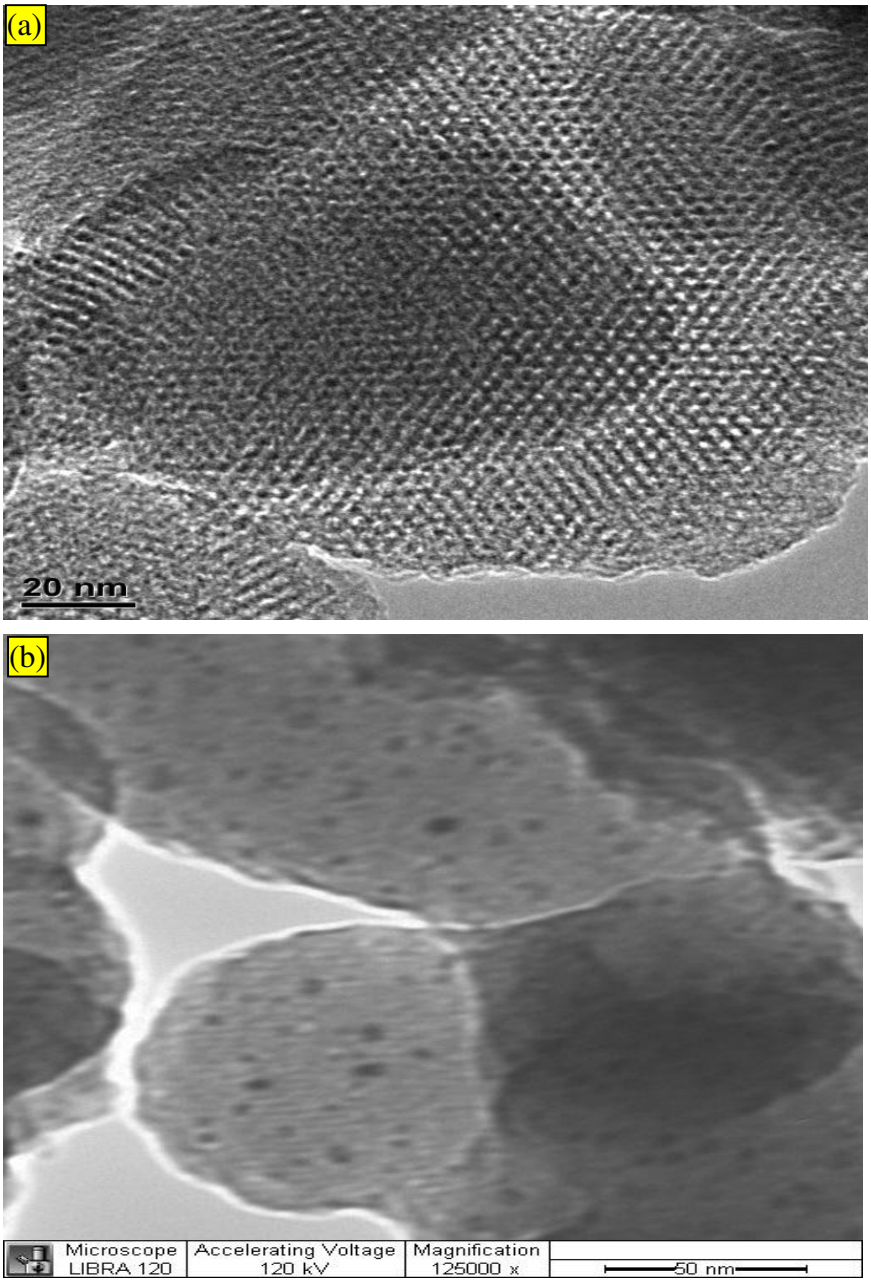

Fig. 5: TEM images of calcined: (a) MCM-41, and (b) Pd-MCM-41 (Pd-black dots)

The uniformly ordered hexagonal pores of MCM-41 evident in the TEM images are consistent with the results of our SAXRD studies discussed previously. The uniform distribution of the Pd

nanoparticles (black/darker dots) in the MCM-41 framework is conspicuous in the TEM image in **Fig. 5(b)**. Further, the experimental metal loading, determined using ICP-OES and EDX analysis (next section) is consistent with theoretical loading and indicate that our optimized one-pot synthesis can be a reliable method for uniform incorporation of metal oxides in MCM-41. The distance between pores is about 3– 4 nm, while the bulk catalyst particle sizes were estimated to be in the range of 2.5 – 60 μm.

3.6. ICP-OES and EDX Spectroscopy

ICP-OES and EDX were used to estimate the actual quantity of metals retained in the calcined samples of MCM-41 catalysts (**Table 2).**

Table 2: Results of monometallic catalysts loading evaluated by ICP-OES and EDX analysis

Catalyst	Intended Metal Loading (wt %)	Metal Loading using ICP (wt %)	Metal Loading using EDX (wt %)
Ni-MCM-41	10	13.8	11.1
Cu-MCM-41	10	8.2	8.2
Pd-MCM-41	10	2.5	3.6
Sn-MCM-41	10	13.4	14.1
Co-MCM-41	10	13.2	10.5
Zn-MCM-41	10	9.9	11.7

The metal loadings determined experimentally were fairly consistent with the theoretical loading except in the case of Pd-samples. We believe this difference was possibly caused by incomplete precipitation of Pd (as hydroxides [$Pd(OH)_2$]) in the mesoporous matrix or possibly due to adventitious loss of metals during the washing step of the catalyst preparation.

3.7. FTIR Spectra Analysis

The changes in bonding properties introduced by metal incorporation in the mesoporous MCM-41 matrix were monitored using FTIR spectroscopy. The typical FTIR spectra of as prepared MCM-41 and calcined M-MCM-41 are shown in **Fig. 6(a)**.

The FTIR peak at ~1500 cm^{-1} is assigned to aliphatic C–H bending vibrations while those peaks in the range of 2600 - 3100 cm^{-1} are assigned to aliphatic C–H stretching vibrations of the surfactant (CTAB) in the as-prepared (non-calcined) MCM-41 support [34]. Consequently, these peaks disappear in the calcined samples implying that the calcination at 550 ºC effectively removed all the surfactant from MCM-41 matrix as expected. The wide absorption band between 3600 and 3200 cm^{-1} could be due to the O-H bond stretching vibrations of silanol groups and/or adsorbed moisture on the support [35]. The intense nature of the O-H peak of the as-prepared samples compared to calcined samples portrays the presence of numerous –OH groups in the matrix that are present under synthesis conditions.

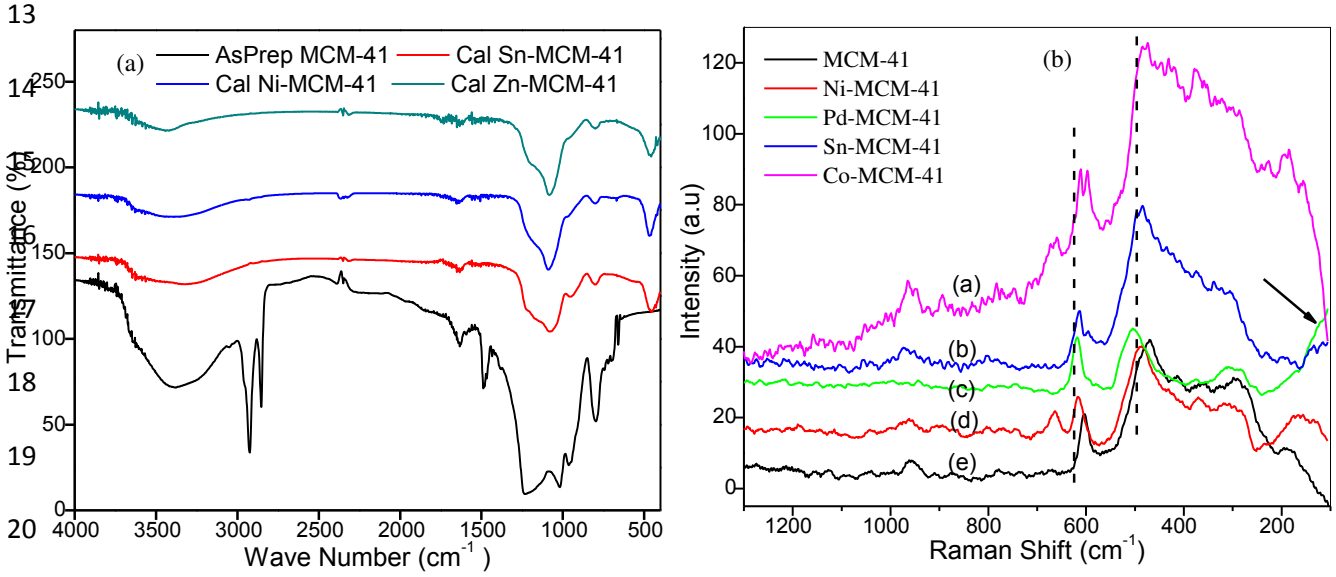

Fig. 6: Typical (a) FTIR and (b) Raman spectra of calcined M-MCM-41catalysts

The bands at 1650 cm^{-1} are caused by bending vibrations of entrapped water molecules in the MCM-41 matrix, and those observed between 800 cm^{-1} and 1000 $cm^{-1}$are assigned to bending and

symmetric stretching vibrations of the Si-O-Si linkages [35, 36]. The bands observed around 1250 cm^{-1} and 1030 cm^{-1} are characteristic peaks of asymmetric Si-O-Si stretching vibrations [21, 37]. The conspicuous absorption peaks around 500 cm^{-1}, present only when the metals were incorporated in the silica support, could be ascribed to the bending vibrations of tetragonal Si-O-Si- bonds [38].

3.8. Laser Raman (LR) Spectra Analysis

The oxides of transition metals are well studied for their strong inelastic Raman scattering due to their inherent molecular symmetry [39]. The Raman technique was therefore used to record vibrational low-frequency modes of the encapsulated metals in the silica framework as a complementary method to the FTIR spectroscopy. The IR active stretching vibrations of surface silanol groups between 3000 and 4000 cm^{-1} and absorption bands around 1600 cm^{-1} were Raman inactive hence not shown. The Raman spectra of M-MCM-41 catalysts in the range of 100-1300 cm^{-1} are shown in **Fig. 6(b)**. The intense IR signals due to Si-O-Si bending and stretching vibrations at 800 cm^{-1} and 1000 cm^{-1} (**Fig. 6(a)**) showed very weak Raman bands. The intense Raman bands at 600 cm^{-1} and 490 cm^{-1} are attributed to the Si-O-Si vibrations of amorphous three membered SiO_4 and the four membered tetrahedral SiO_4 rings, respectively [40-42]. The presence of free surface silanols is revealed by band at 960 cm^{-1} attributed to the Si-OH stretching vibrations [41]. A slight redshift of about 10-30 cm^{-1} was noticed for both bands upon incorporation of the metals in the MCM-41 framework. These nominal shifts could be due to an appreciable decrease in the bond strength and/or bond angle caused by the formation of oxygen-metal-oxygen (O-M-O) bridges in the silica framework [43]. This observation suggest possible modifications in the MCM-41 structure induced by the metal presence.

3.9. H_2-TPR Studies of Metal-Support Interactions and Reducibility of Calcined Samples

Temperature programmed reduction (TPR) is a very useful technique for evaluating the strength of metal-support interactions , specifically between the metal oxides and the support as well as determining the ease of reducibility of the metal oxides (Hurst et al [44]). The TPR profiles in 10% H_2/Ar of M-MCM-41 catalysts calcined at 550 °C are shown in **Fig. 7**.

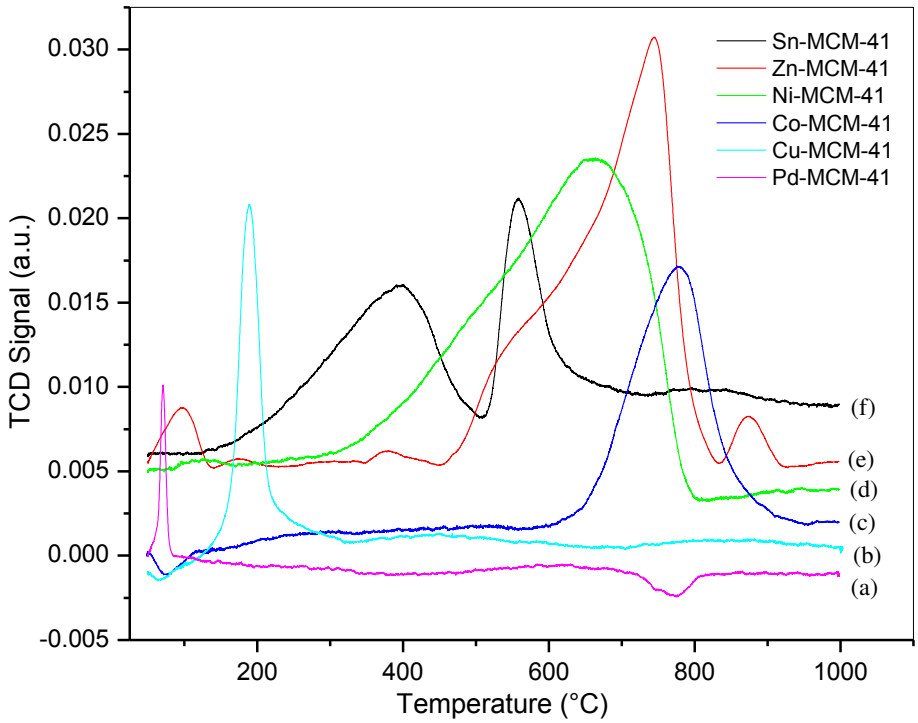

Fig. 7: H_2-TPR profiles of M-MCM-41 catalysts: (a) Pd, (b) Cu, (c) Co, (d) Ni, (e) Zn, and (f) Sn

The reduction of CuO to Cu^0 began at 100 °C and attained a maximum peak at 200 °C. This concurred with observation reported by Matsumura and Vizcaino et al [45, 46], wherein Cu supported on commercial silica and ZSM were investigated for their methanol and ethanol steam reforming activities, respectively. They ascertained that reduction of CuO to Cu^0 occurred in a similar temperature range. Nonetheless, the fact that the bulk CuO was reduced in the temperature range of 200 °C < *T*r < 300 °C [47-49], suggests that the relatively lower Cu reduction temperature

of our sample was caused by good dispersion of relatively small sizes of the CuO crystallites as evident in the EDX mapping discussed before.

The TPR of Pd-MCM-41 sample (**Fig. 7**) showed the greatest ease of reducibility among the synthesized catalysts. A sharp peak for hydrogen consumption that can be ascribed to PdO reduction was noticed at ~95 °C followed by a small negative peak at ~780 °C ascribed to the hydrogen release confirming the inherent ability of palladium to strongly absorb hydrogen inside the interstitial cavities of the metal lattice (face-centered cubic structure) to form polymorphs of palladium hydride [50]. The observed TPR profile of PdO is similar to that obtained by Chou et al [51]. At lower temperatures (< 100 °C), palladium crystallites extract hydrogen atoms to form the beta PdH phases which decomposes spontaneously (and desorb the hydrogen atoms) at temperatures > 633 °C to form the alpha PdH phase**.** They also reported that the reduction temperature of bulk PdO species under hydrogen stream is generally low (-100 °C < *T*r < 60 °C). In contrast to PdO, reduction of NiO to Ni^0 occurred in a slow progressive pattern between 300 and 900 °C. The broadness of the peak suggested that the NiO crystallites had different sizes which interacted differently with the support leading to hydrogen consumption over wide range of temperature [52].

While the metal-support interactions have been well established in catalysts with reducible supports (e.g. TiO_2)[53, 54], for inert supports (e.g. SiO_2) several contradictory studies have been reported claiming presence and absence of metal-support interactions [14, 54-59]. Furthermore, most of studies indicated that the presence of metal support interactions in SiO_2 supported catalysts were limited to only few metals, especially, Co, Ni, Pt and Pd. The formation of non- or high temperature reducible surface compounds such as nickel silicides, cobalt silcates, Pt silicides, and Pd silicides were mainly attributed to the metal-support interactions [57-60]. For Ni-MCM-

41, in this study, most of the NiO is reduced above 550 °C with reduction peak centered at ~650 °C. This is consistent with reported studies where lower temperature reduction part is attributed to smaller NiO particles and the major peak centered at ~650 °C corresponds to reduction of Ni silicides [18, 30]. Similar to Ni-MCM-41, Co-MCM-41 is also reduced at temperature centered at 780 °C, indicating the possible formation of cobalt silicates which are known to be reduced at inordinately higher temperatures [61, 62]. It should be noted that Ni-MCM-41 and Co-MCM-41both showed least dispersion (**Fig. 4**) compared to other MCM-41 catalysts and Ni-TiO_2 and Co-TiO_2 catalysts in our earlier study [53]. The noticeable better dispersion of Ni and Co in TiO_2 was attributed to better metal-support interactions. More specifically, we observed complete reduction of NiO in Ni-TiO_2 catalysts by 600 °C with main peak centered at just 400 °C [49]. This is much lower than that observed with the SiO_2 matrix. The significant shift in reduction temperature for Ni-TiO_2 catalysts was attributed to metal-support interactions between NiO and TiO_2. Thus, it can be inferred that the metal-support interaction is more complex and may not be determined only on the basis of surface compound formation that are reduced at high temperature.

In contrast to Co-MCM-41, Sn-MCM-41 registered two distinct hydrogen uptake peaks centered at about 400 °C and 570 °C which could be ascribed to the reduction of SnO_2 and SnO nanocrytallites, respectively [19]. ZnO exhibited three distinct reduction phases. The reduction temperature of bulk ZnO particles is reported around 650 °C [63, 64]. The small reduction peak around 100 °C could therefore be attributed to few nanocrystalline bulk ZnO particles. The more intense peak at 750 °C is due to reduction of the majority of bulk ZnO species. The small peak centered at ~850 °C may be ascribed to reduction of small amounts of very stable silicates in the matrix [65]. In contrast, the significant portion of ZnO in Zn-TiO_2 in earlier study was observed to be reduced in the temperature range of 300-500 °C [53] owing to better metal-support

interaciton. Thus, the observation of typical reduction profile of Zn-MCM-41 indicates the absence of any significant metal-support inteactions between ZnO and SiO_2.

4. SRM Activity and Selectivity Evaluation of M-MCM-41 Catalysts

In order to examine the comparative performance of Co, Cu, Ni, Pd, Sn and Zn in MCM-41 (M-MCM-41), steam reforming of methanol was carried out under identical operating conditions. Methanol conversion and selectivity to H_2, CO, CO_2 and CH_4 were measured for each M-MCM-41 catalyst at four selected temperatures, 200, 250, 300 and 350 °C. In our experiments, no intermediate products such as formic acid, formaldehyde, dimethyl ether or methyl formate were detected. We assumed the following main reactions in steam reforming of methanol:

Methanol Decomposition: $CH_3OH \rightarrow 2H_2 + CO \ \Delta H = 90.6 kJ/mol$ (5)

Water Gas Shift Reaction: $CO + H_2O \leftrightarrow H_2 + CO_2 \ \Delta H = -41.2 kJ/mol$ (6)

Overall Reaction: $CH_3OH + H_2O \rightarrow 3H_2 + CO_2 \ \Delta H = 49.5 kJ/mol$ (7)

Methanation Reaction: $CO + 3H_2 \rightarrow CH_4 + H_2O \ \Delta H = -206 \ kJ/mol$ (8)

Table 3 shows methanol conversion and product selectivity of the SRM by each catalyst. As expected for an endothermic reaction, methanol conversion increased with increase in temperature for each M-MCM-41 catalyst.

Table 3: Methanol conversion and product gas selectivities of M-MCM-41 supported catalysts

Catalyst	Temperature (°C)	Conversion (%)	Selectivity (%)			
			H_2	CO	CO_2	CH_4
Co-MCM-41	200	6.4	99.1	21.3	69.0	9.7
	250	12.1	98.9	18.0	77.5	4.5
	300	14.4	98.2	28.4	63.6	8.0
	350	38.2	96.2	44.7	44.6	10.7
Pd-MCM-41	200	46.4	99.2	93.5	5.7	0.8
	250	51.9	97.8	77.3	18.0	4.7
	300	69.0	98.5	73.7	19.4	6.9

	350	73.4	98.4	69.4	24.5	6.1
Zn-MCM-41	200	15.7	91.9	35.6	40.8	23.6
	250	18.6	94.9	34.1	52.5	13.4
	300	35.6	98.5	28.5	55.1	16.4
	350	47.4	98.6	15.3	61.2	23.5
Cu-MCM-41	200	53.9	100	4.2	95.8	0
	250	67.8	100	5.6	94.4	0
	300	69.9	100	16.4	83.6	0
	350	82.3	99.5	17.7	81.3	1.0
Sn-MCM-41	200	21.0	94.6	32.1	24.1	43.8
	250	27.2	76.9	16.7	30.9	52.4
	300	39.1	74.8	13.9	27.1	59.0
	350	42.2	64.0	12.6	29.5	57.9
Ni-MCM-41	200	13.3	100	92.5	7.5	0
	250	19.7	99.7	94.9	4.7	0.4
	300	22.1	99.6	95.4	4.1	0.5
	350	45.1	99.9	99.0	0.9	0.1

The overall SRM reactivity trend for different metals based on methanol conversion followed the order of Cu > Pd > Sn > Ni ≈ Zn > Co with Cu-MCM-41 displaying the highest ~82% methanol conversion at 350 °C. However, if the catalyst performance is normalized based on the actual metal loading, Pd completely outperformed Cu among the two best catalysts. The relative SRM catalytic superiority of Pd and Cu catalysts are consistent with the results of Eswaramoorthi and Dalai [66] as well as Valdes-Solis et al. [67]. Eswaramoorthi and Dalai reported that at 300 °C, SBA-15 supported 4.5wt% Pd catalyst yielded as high as 86% methanol conversion. Valdes-Solis et al. concluded that at 250 °C, Cu catalysts showed initial high kinetic SRM activity. Compared to Cu and Ni, other metal (Zn, Sn, Ni and Co) showed almost half the methanol converions. The lower activity showed by Co-MCM-41 (14% and 38 % at 300 and 350 °C, respectively) and Ni-MCM-41 (22% and 45 % at 300 and 350 °C, respectively) could be attributed to their significantly lower reducibility owing to the silicates and silicides formation as discussed in the TPR studies (**Fig. 7, and section above**). The observed overall activity are consistent with most of the reported studies which have indicated that Cu and Pd based catalysts are most active

for steam reforming [66, 67]. However, it should be noted that when mesoporous TiO_2 was used a support in our earlier study, Zn and Ni showed showed significantly higher activity compared to Cu. This was attributed to the metal-support interactions leading to the lower reducibility of Zn and Ni in TiO_2 matrix [53]. On the other hand, as observed in TPR analysis with MCM-41, the metal particles seem to behave like bulk materials with advantage of higher surface area.

The selectivities of the product gases were quite different for each catalytic system. All the catalysts displayed over 96% selectivity towards H_2 except Sn-MCM-41 that showed a moderate 78% average H_2 selectivity. While Cu-MCM-41and Ni-MCM-41showed very little selevtivity (0-0.5%) towards methane (undesirable product in this study), Sn-MCM-41 exhibited the highest CH_4 methane selectivity (~58%). This explains the observed lower H_2 selectivity for Sn at each reaction temperature; the formation of a mole of CH_4 consumes 3 moles of H_2 **(Eq. 5)**. In our recent study with different Cu loadings in Cu-MCM-41, we showed that there is always some activity for methanation reaction; however, at sufficient Cu loading, reforming of formed CH_4 during SRM ($CH_4 + H_2O \rightarrow CO + 3H_2$) is a dominating reaction, thus producing only 0-1% of CH_4 [21]. This could also be the reason for the lower CH_4 selectivity of Ni-MCM-41 although it is a good methanation catalyst. For Pd and Co, it could either be the same reason as for Cu or the lower methanation activity observed for lower CH_4 selectivity.

The selectivity towards CO production showed profound variations for different M-MCM-41 catalysts. The observed trend was Cu < Sn < Co < Zn < Pd < Ni. While the observed lower CO selectivity for Cu can be attributed to the better water gas shift reaction (WGSR) activity, for Sn it is due to the higher methanatin activity. It is interesting to note that, on one hand, Cu which showed least CO selectivity (e.g. 5.6% at 250 °C) when supported in MCM-41, TiO_2 supported Cu showed significantly higher CO selectivity (e.g. 57% at 250 °C). On the other hand, Zn-TiO_2 showed

considerably lower CO selectivity, 3%, compared to 34% by Zn-MCM-41 [53]. The Pd and Ni showed least CO selectivities among the different studied metals when supported both in MCM-41 and TiO_2, ascribed to the lower WGSR activity [53]. These results clearly indicate the role of specific metal-support interactions in different metal-support systems.

4.1 Stability Test of M-MCM-41 Catalysts for SRM

The stability of the M-MCM-41 catalysts was examined to substantiate their ability to resist deactivation. This was carried out by running freshly reduced samples on stream continuously for 40 h. The experiments were performed at 300 °C under identical experimental conditions described previously in section 2.4. The methanol conversion for each M-MCM-41 catalyst over a period of 40 h on stream is presented in **Fig. 8.**

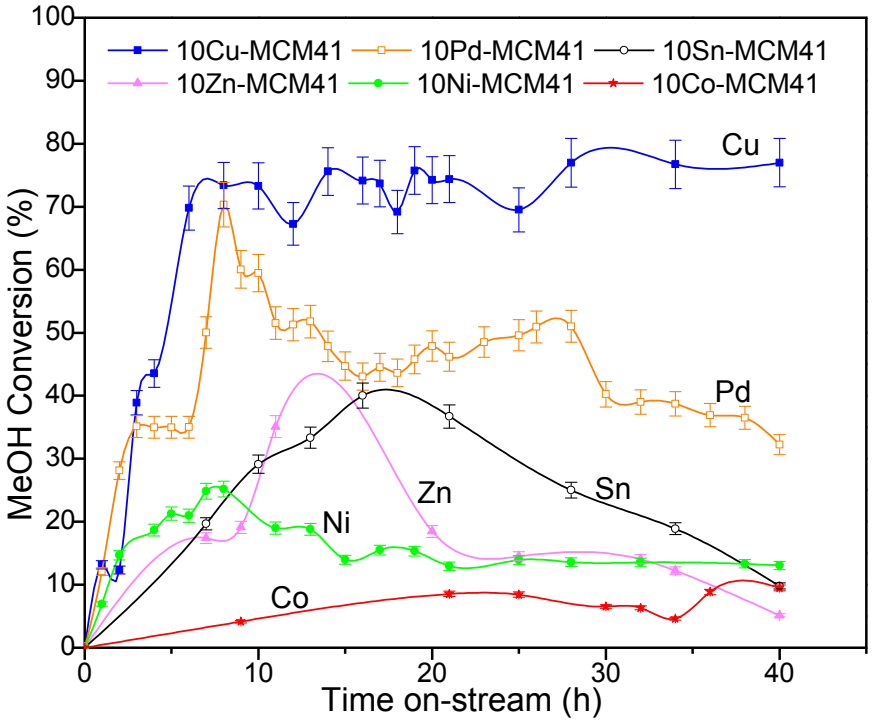

Fig. 8: Catalysts activity as a function of time on-stream during SRM. Reaction conditions: 300 °C, 1 atm, methanol/water molar ratio of 1/3 and a GHSV of 2838 h^{-1}at STP

The initial increase in conversion with time is due to the unsteady state which was different for different catalysts. The trend of activity for 40 h on stream was similar to SRM catalytic performance discussed in **section 4** (Cu > Pd > Sn > Ni ≈ Zn > Co). Cu-MCM-41 was observed to be the most stable, maintaining ~74% conversion and no apparent signs of deactivation for 10 to 40 h. Except for Cu-MCM-41 and Co-MCM-41, all other catalysts showed decline in conversion after attaining the short steady state with respective highest conversions. Although, Co-MCM-41 showed no decline in conversion, it was always less than 10% until the end of 40 h. For Ni-MCM-41, after initial decline, the conversion was steadied at 14%. However, for Pd, Zn and Sn, the conversion kept decreasing with time-on-steam, indicating continuous deactivation over the time. For example, methanol conversion for Pd-MCM-41 decreased rapidly to ~30%, representing less than 50% SRM activity compared to that of Cu-MCM-41 at the end of 40 h. Sn and Zn also showed a decline in methanol conversion to ~20% and ~30%, respectively, for the period of 10-40 h on stream. The effect of time-on-stream on the selectivities of the product gas mixture is presented in **Fig. S1** (supplemental information)**.** Duration on stream did not seem to have any dramatic effect on the selectivities of H_2, CO, CH_4 and CO_2 except that the CH_4 selectivity for Sn-MCM-41 started to decrease significantly after 20 h reaching about 18% at the end of 40 h.

4.2 Characterization of Spent M-MCM-41 Catalysts

Characterization of spent catalysts after SRM reactions was carried out to investigate the effect of reaction time on the physicochemical properties and the possible causes of deactivation of the catalysts. The SAXRD and WAXRD patterns of spent catalysts are shown in **Fig. 9** (a) and (b), respectively.

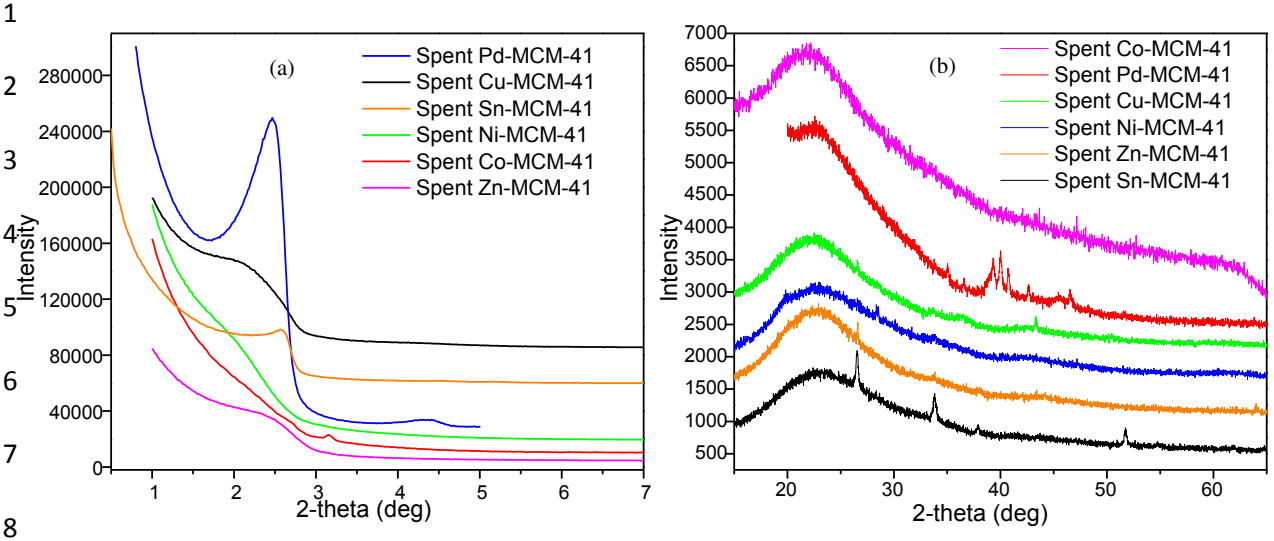

Fig. 9: (a) Small angle and (b) wide angle XRD diffraction profiles of spent catalysts

Fig. 9(a) showed that SAXRD peak intensity for all the spent catalysts except that of spent Pd-MCM-41 decreased drastically comparted to fresh catalysts indicating deterioration of the ordered structure after the 40 h time-on-stream experiments. The BET surface areas of the spent catalysts shown in **Table 1** are consistent with SAXRD results. After 40 h on-stream, all the catalysts retained an appreciable surface area. Pd-MCM-41 showed ~32% decrease in surface area while Co and Cu recorded the highest decline of ~44%. Concomitantly about 15 - 30% loss of total pore volume was observed for all spent catalysts. With the exception of Zn-MCM-41, that lost ~25% of its pore size, all other catalysts essentially maintained their pore morphology; hence some degree of ordered mesoporosity. Thus, the results indicate that the M-MCM-41 catalysts have issues in terms of hydrothermal stability under the reaction conditions.

The WAXRD patterns of the spent catalysts shown in **Fig. 9(b)** were essentially similar to the fresh catalysts with slight modifications. The noticeable differences were observed in WAXRD profiles of fresh **(Fig. 3(b))** and spent (**Fig. 9(b)**) Pd-MCM-41, Cu-MCM-41 and Sn-MCM-41 catalysts. The diffraction peak of PdO centered at 2θ value of 33.9° indexed to (101) as well as the

35.6º and 38.9º peaks of CuO crystallites in the fresh catalysts disappeared after 40 h of reaction. The emergence of new moderate intensity diffraction peaks (2θ = 38.5º, 39.3º, 40 º) for Pd-MCM-41 indicated structural transformation after 40h of SRM. While the diffraction peak at 2θ around 40º is indexed to (111) reflections of the PdO-crystallites [68, 69]; those at 38.5º, and 39.3º are attributed to the formation of palladium carbide (Pd-C) [70-72]. The researchers showed that in the presence of carbon containing gases, Pd reacts (even < 200 °C) with carbon to form a metastable Pd-C phase. The moderately intense oxide diffraction peak of Sn and the very weak ones of Zn, Ni, Cu at $2\theta = 26.8 - 29.4^{o}$ indicated crystallographic traces of carbon (002) reflections [73-75]. For Sn-MCM-41, a significant increase in crystallinity of the Sn oxides was observed. The appearance of strong peaks at 2θ = 26.8°, 34.2°, 38.5°, 52.2° are indexed to the SnO_2 (110), (101), (200), (211) crystallographic planes, respectively [76]. The SnO_2 crystal size calculated using Eq. (1) was 33.8 nm. The appearance of the SnO_2 peaks in the spent Sn-MCM-41catalysts suggests possible thermal sintering of the SnO/SnO_2 oxides.

In order to estimate the extent of coke deposition the spent catalysts were subjected to TGA-DSC under air environment. TGA-DSC themograms displayed in **Fig. S2** indicated that spent catalysts recorded a nominal 0.25% - 0.96% coke formation between 400 °C and 570 °C that has usually been attributed to amorphous and graphitic carbon [16, 77]. It should be noted that Zn-MCM-41 and Cu-MCM-41 showed the lowest temperature of coke oxidation among different catalysts indicating amorphous nature of the deposited coke. The absence of cleavable C-C bonds in methanol suggests the carbon deposit most likely occurred by the disproportionation of carbon monoxide (Boudouard reaction) $2CO \rightarrow CO_2 + C$ [78, 79]. In order to determine the role of coke in the catalyst deactivatin, we activated the spent Pd-MCM-41 (40 h time-on-stream) as a representative catalyst in-situ using air. The reuse of the activated catalyst for SRM showed

complete recovery of catalyst activity. This indicates that coking plays a major role in the deactivation of the catalysts. The absence of coke effect on Cu-MCM-41 activity could be attributed to the amorphous nature of the coke. However, given the amorphous nature of coke, the decreased activity of Zn-MCM-41 suggests that although coke deposition seems to be major cause of deactivation, other mechanisms such as structural degradation and sintering may also be contributing to the catalysts deactivation.

5. Conclusions

Comparative performances of Cu, Co, Ni, Pd, Zn, and Sn catalysts incorporated in high surface area MCM-41 matrix were investigated for methanol steam reforming. These catalysts were synthesized using an optimized one pot hydrothermal procedure. The small angle XRD and N_2 adsorption-desorption studies corroborated the ordered structure of the MCM-41 matrix and the retention of the ordered structure after incorporation of 10 wt% of the metals. Of all the catalysts studied, Cu-MCM-41 and Pd-MCM-41 exhibited dominant SRM activity. Cu-MCM-41 showed the best catalytic performance with 68% methanol conversion and100% H_2, 6% CO selectivity with no noticeable CH_4 formation at ~ at 250 °C While Cu-MCM-41 strongly enhanced the WGSR, Pd-MCM-41 and Ni-MCM-41 catalysts showed least activity for WGSR resulting in higher CO selectivities. With regards to catalysts stability, Cu/MCM41 was the most stable and displayed consistent steady state conversion (up to74%) over 40 h time-on-stream. Although coking played an influential role in deactivation of most catalysts, thermal sintering and changes in MCM-41 structure also could be responsible for the catalyst deactivation. Comparision of M-MCM-41 characteristics and SRM performance over M-TiO_2 in our earlier studies suggest that metal particles in MCM-41 behave like bulk materials having no significant metal-support interaction as observed in M-TiO_2 catalysts.

Acknowledgement

The authors express their profound gratitude to the National Science Foundation (NSF) for funding the NSF-CREST Bioenergy Center (Grant No. HRD-124215). Our sincere gratitude goes to Dr. Keith Schimmel (EES Dept. Chairperson) for his financial assistance. We would like to thank Mr James King (Chemistry Department) for supporting our experimental work and Mr. Bryce Holmes (School of Agriculture and Environmental Sciences) for his assistance with ICP-OES analysis. The authors thank Dr. Sankar and Dr. Yarmolenko (Center for Advanced Materials and Smart Structures-CAMSS) at NCAT for the use of their XRD for material characterization. Finally, we thank Dr. Abolghasem Shahbazi (Biological and Chemical Engineering Dept. Chairperson) and Dr. Lijun Wang for the use of his Chemical Analyzer for TPR and TGA studies and Dr. Shamsuuddin Illias (Chemical Engineering Department) for his assistance with BET analysis.

References

[1] S. Sá, H. Silva, L. Brandão, J.M. Sousa, A. Mendes, Appl. Catal. B Environ. 99 (2010) 43-57.

[2] D.R. Palo, R.A. Dagle, J.D. Holladay, Chem. Rev. 107 (2007) 3992-4021.

[3] B. Lorenzut, T. Montini, L. De Rogatis, P. Canton, A. Benedetti, P. Fornasiero, Appl. Catal. B Environ. 101 (2011) 397-408.

[4] L. Zhang, L. Pan, C. Ni, T. Sun, S. Zhao, S. Wang, A. Wang, Y. Hu, Int. J. Hydrogen Energy. 38 (2013) 4397-4406.

[5] P. Hirunsit, K. Faungnawakij, J. Phys. Chem. C. 117 (2013) 23757-23765.

[6] A. Jomekian, S.A.A. Mansoori, B. Bazooyar, A. Moradian, J. Porous Mater. 19 (2012) 979-988.

[7] G. Wang, Z. Liu, Y. Liu, G. Liu, M. Xu, L. Wang, Chin. J. Catal. 29 (2008) 1159-1164.

[8] V. Nichele, M. Signoretto, F. Menegazzo, A. Gallo, V. Dal Santo, G. Cruciani, G. Cerrato, Appl. Catal. B Environ. 111 (2012) 225-232.

[9] R.Y. Abrokwah, V.G. Deshmane, D. Kuila, Adv. Mater. Res. 1096 (2015) 161-168.

[10] K. Kosaraju, A. Rahman, M. Duncan, B. Tatineni, Y. Basova, V. Deshmane, R. Abrokwah, S. Hosseinnezhad, J. King, S. Ilias, Future Energy Environ. Mater. 88 (2014) 337-344.
[11] E. Yamamoto, K. Kuroda, Bull. Chem. Soc. Jpn. 89 (2016) 501-539.
[12] V. Malgras, Q. Ji, Y. Kamachi, T. Mori, F.-K. Shieh, K.C.-W. Wu, K. Ariga, Y. Yamauchi, Bull. Chem. Soc. Jpn. 88 (2015) 1171-1200.
[13] N. Song, Y.-W. Yang, Chem. Soc. Rev. 44 (2015) 3474-3504.
[14] R. Riva, H. Miessner, R. Vitali, G. Del Piero, Appl. Catal. A Gen. 196 (2000) 111-123.
[15] A.N. Fatsikostas, D.I. Kondarides, X.E. Verykios, Catal. Today. 75 (2002) 145-155.
[16] D. Liu, R. Lau, A. Borgna, Y. Yang, Appl. Catal. A Gen. 358 (2009) 110-118.
[17] E. Ozdogan, T. Dogu, G. Dogu, Int. J. Chem. Reactor Eng. 5 (2007) 1-11.
[18] L. Bobadilla, S. Palma, S. Ivanova, M. Domínguez, F. Romero-Sarria, M. Centeno, J. Odriozola, Int. J. Hydrogen Energy. 38 (2013) 6646-6656.
[19] J.S. Lee, G.B. Han, M. Kang, Energy. 44 (2012) 248-256.
[20] A. Ota, E.L. Kunkes, I. Kasatkin, E. Groppo, D. Ferri, B. Poceiro, R.M.N. Yerga, M. Behrens, J. Catal. 293 (2012) 27-38.
[21] V.G. Deshmane, R.Y. Abrokwah, D. Kuila, Int. J. Hydrogen Energy. 40 (2015) 10439-10452.
[22] M. Jaroniec, L.A. Solovyov, Langmuir. 22 (2006) 6757-6760.
[23] M. Ugalde, E. Chavira, M. Ochoa-Lara, I. Figueroa, C. Quintanar, A. Tejeda, J. Nanotech. 2013 (2013).
[24] L. Huang, Y. Wang, Z. Wang, F. Chen, J. Tan, P.K. Wong, Phys. Chem. 2 (2012) 27-34.
[25] P.S.S. Reddya, N.S. Babua, N. Lingaiaha, P.S. Prasada, I. Raob, Europian Congress of Chemical Engineering, Copenhagen, Denmark, 2007, pp. 1-12.
[26] R. Singh, S. Kulkarni, N. Naik, Adv. Mater. Lett. 4 (2013) 82-88.
[27] C. Li, S. Liu, J. Nanomater. 2012 (2012) 1-6.
[28] N.C. Pramanik, S. Das, P.K. Biswas, Mater. Lett. 56 (2002) 671-679.
[29] S. Biz, M.L. Occelli, Catal. Rev. 40 (1998) 329-407.
[30] D. Liu, X.Y. Quek, W.N.E. Cheo, R. Lau, A. Borgna, Y. Yang, J. Catal. 266 (2009) 380-390.
[31] S.Z. Islam, V.G. Deshmane, S. Ilias, Sep. Sci. Technol. (2015).
[32] M. Zienkiewicz-Strzałka, S. Pikus, Appl. Surf. Sci. 261 (2012) 616-622.

[33] J. Panpranot, K. Pattamakomsan, J.G. Goodwin Jr, P. Praserthdam, Catal. Commun. 5 (2004) 583-590.
[34] S. Chaliha, K.G. Bhattacharyya, J. Hazard. Mater. 150 (2008) 728-736.
[35] F. Adam, T.-S. Chew, The Open Colloid Sci. J. 5 (2012) 1-4.
[36] V.G. Deshmane, Y.G. Adewuyi, Microporous Mesoporous Mater. 148 (2012) 88-100.
[37] N.I. Taib, S. Endud, M.N. Katun, Int. J. Chem. 3 (2011) 2.
[38] C. Huo, J. Ouyang, H. Yang, Sci. Rep. 4 (2014) 1-9.
[39] Z. Zhang, J. Suo, X. Zhang, S. Li, Appl. Catal. A Gen. 179 (1999) 11-19.
[40] E.L. Lee, I.E. Wachs, J. Phys. Chem. C. 112 (2008) 6487-6498.
[41] Y. Borodko, J.W. Ager, G.E. Marti, H. Song, K. Niesz, G.A. Somorjai, J. Phys. Chem. B. 109 (2005) 17386-17390.
[42] Z. Zhang, Y. Han, F.-S. Xiao, S. Qiu, L. Zhu, R. Wang, Y. Yu, Z. Zhang, B. Zou, Y. Wang, J. Am. Chem. Soc. 123 (2001) 5014-5021.
[43] I.E. Wachs, Catal. Today. 27 (1996) 437-455.
[44] N.W. Hurst, S.J. Gentry, A. Jones, B.D. McNicol, Catal. Rev. Sci. Eng. 24 (1982) 233-309.
[45] Y. Matsumura, H. Ishibe, Appl. Catal. B Environ. 86 (2009) 114-120.
[46] A. Vizcaíno, A. Carrero, J. Calles, Int. J. Hydrogen Energy. 32 (2007) 1450-1461.
[47] L. Kundakovic, M. Flytzani-Stephanopoulos, Appl. Catal. A Gen. 171 (1998) 13-29.
[48] P. Barnes, M. Tiernan, G. Parkes, J. Therm. Anal. Calorim. 56 (1999) 733-737.
[49] M. Rafati, L. Wang, A. Shahbazi, J. CO2 Utilization. 12 (2015) 34-42.
[50] B.D. Adams, A. Chen, Mater. Today. 14 (2011) 282-289.
[51] C.-W. Chou, S.-J. Chu, H.-J. Chiang, C.-Y. Huang, C.-j. Lee, S.-R. Sheen, T.P. Perng, C.-t. Yeh, J. Phys. Chem. B. 105 (2001) 9113-9117.
[52] B. Pawelec, S. Damyanova, K. Arishtirova, J.L.G. Fierro, L. Petrov, Appl. Catal. A Gen. 323 (2007) 188-201.
[53] V.G. Deshmane, S.L. Owen, R.Y. Abrokwah, D. Kuila, J. Mol. Catal. A: Chem. 408 (2015) 202-213.
[54] J. Van de Loosdrecht, A. Van der Kraan, A. Van Dillen, J. Geus, J. Catal. 170 (1997) 217-226.

[55] W.-J. Shen, M. Okumura, Y. Matsumura, M. Haruta, Appl. Catal. A Gen. 213 (2001) 225-232.
[56] J.P. Bucher, J. Van der Klink, M. Graetzel, J. Phys. Chem. 94 (1990) 1209-1211.
[57] C. Hippe, R. Lamber, G. Schulz-Ekloff, U. Schubert, Catal. Lett. 43 (1997) 195-199.
[58] E. van Steen, G.S. Sewell, R.A. Makhothe, C. Micklethwaite, H. Manstein, M. de Lange, C.T. O'Connor, J. Catal. 162 (1996) 220-229.
[59] T. Ueckert, R. Lamber, N. Jaeger, U. Schubert, Appl. Catal. A Gen. 155 (1997) 75-85.
[60] R. Lamber, N. Jaeger, G. Schulz-Ekloff, J. Catal. 123 (1990) 285-297.
[61] F. Boubekr, A. Davidson, S. Casale, P. Massiani, Microporous Mesoporous Mater. 141 (2011) 157-166.
[62] N. Osakoo, R. Henkel, S. Loiha, F. Roessner, J. Wittayakun, Appl. Catal. A Gen. 464 (2013) 269-280.
[63] R. Kam, C. Selomulya, R. Amal, J. Scott, J. Catal. 273 (2010) 73-81.
[64] S. Lew, A. Sarofim, M. Flytzani-Stephanopoulos, Chem. Eng. Sci. 47 (1992) 1421-1431.
[65] S.-W. Park, O.-S. Joo, K.-D. Jung, H. Kim, S.-H. Han, Appl. Catal. A Gen. 211 (2001) 81-90.
[66] I. Eswaramoorthi, A. Dalai, Int. J. Hydrogen Energy. 34 (2009) 2580-2590.
[67] T. Valdes-Solis, G. Marban, A. Fuertes, Catal. Today. 116 (2006) 354-360.
[68] C.-M. Lin, T.-L. Hung, Y.-H. Huang, K.-T. Wu, M.-T. Tang, C.-H. Lee, C. Chen, Y. Chen, Physical Review B. 75 (2007) 125426.
[69] S. Moisan, V. Martinez, P. Weisbecker, F. Cansell, S. Mecking, C. Aymonier, J. Am. Chem. Soc. 129 (2007) 10602-10606.
[70] S. Ordóñez, F.V. Díez, H. Sastre, Appl. Catal. B Environ. 31 (2001) 113-122.
[71] E. Van de Sandt, A. Wiersma, M. Makkee, H. Van Bekkum, J. Moulijn, Appl. Catal. A Gen. 155 (1997) 59-73.
[72] S. Ziemecki, G. Jones, D. Swartzfager, R. Harlow, J. Faber Jr, J. Am. Chem. Soc. 107 (1985) 4547-4548.
[73] F.D. Nayeri, S. Darbari, E.A. Soleimani, S. Mohajerzadeh, J. Phys. D: Appl. Phys. 45 (2012) 285101-285111.
[74] C.K. Cheng, S.Y. Foo, A.A. Adesina, Catal. Today. 164 (2011) 268-274.

[75] K.M. Hardiman, T.T. Ying, A.A. Adesina, E.M. Kennedy, B.Z. Dlugogorski, Chem. Eng. J. 102 (2004) 119-130.

[76] G. De, R. Köhn, G. Xomeritakis, C.J. Brinker, Chem. Commun. (2007) 1840-1842.

[77] S. Arepalli, P. Nikolaev, O. Gorelik, V.G. Hadjiev, W. Holmes, B. Files, L. Yowell, Carbon. 42 (2004) 1783-1791.

[78] N. Laosiripojana, S. Assabumrungrat, J. Power Sources. 163 (2007) 943-951.

[79] M.V. Twigg, M.S. Spencer, Top. Catal. 22 (2003) 191-203.

GRAPHICAL ABSTRACT